POLITECNICO DI TORINO
Repository ISTITUZIONALE

A study of frictional contact effects on modal dissipation characteristics in a debonded structure

Original
A study of frictional contact effects on modal dissipation characteristics in a debonded structure / Kiasat, S., Filippi, M., Salehzadeh Nobari, A., Carrera, E.. - In: INTERNATIONAL JOURNAL OF NON-LINEAR MECHANICS. - ISSN 0020-7462. - 188:(2026). [10.1016/j.ijnonlinmec.2026.105389]

Availability:
This version is available at: 11583/3015166 since: 2026-09-04T14:18:27Z

Publisher:
Elsevier

Published
DOI:10.1016/j.ijnonlinmec.2026.105389

Terms of use:

This article is made available under terms and conditions as specified in the corresponding bibliographic description in the repository

Publisher copyright

(Article begins on next page)

12 October 2026

International Journal of Non–Linear Mechanics 188 (2026) 105389

Contents lists available at ScienceDirect

International Journal of Non-Linear Mechanics

journal homepage: www.elsevier.com/locate/nlm

A study of frictional contact effects on modal dissipation characteristics in a debonded structure

S. Kiasat [a], M. Filippi [a,*], Ali S. Nobari [b,c,*], E. Carrera [a]

[a] Politecnico di Torino, Department of Mechanical and Aerospace Engineering, MUL2 Group, Turin, 10129, Italy
[b] ESDU-ACCURIS, London, United Kingdom
[c] Imperial College London, Department of Aeronautics, London, United Kingdom

ARTICLE INFO

Keywords:
Debonding
Frictional contact
Nonlinear dynamics
Friction-induced damping
Vibration-based structural health monitoring

ABSTRACT

Interlaminar debonding modifies the dynamic behavior of laminated structures by altering stiffness, modal characteristics, and associated dissipation mechanisms. Among these, interfacial friction plays an important but still insufficiently understood role in modal damping variations, particularly in nonlinear regimes.

This study examines the nonlinear dynamic response of a beam with interlaminar debonding, with particular emphasis on friction-induced modal damping and the contribution of superharmonic components. A time–frequency framework is employed to characterize frictional dissipation through reconstructed hysteresis loops, and a pseudo-modal damping index is defined based on the modal strain energy. Finite element simulations incorporating contact and Coulomb friction are used to investigate the effects of friction level, debonding pattern, size, and position.

The results show that frictional contact introduces clear nonlinear features that substantially modify the modal dissipation pattern. In addition, dissipation varies non-monotonically with friction level, indicating the existence of optimal conditions for maximizing hysteretic energy loss. Parametric analyses further reveal that the orientation, location, and size of the debonded region strongly influence friction-induced modal damping and damage-sensitive vibration features.

The proposed framework provides a modal-based interpretation of friction-driven damping by accounting for superharmonic contributions and establishes a foundation for the development of vibration-based damage-detection and structural health-monitoring strategies.

1. Introduction

Interlaminar debonding, defined as the separation of adjacent layers in laminated structures [1,2], is a critical damage mode that significantly compromises structural integrity. This separation, which may originate from manufacturing imperfections or in-service loading, reduces the global stiffness [3,4] and shortens the fatigue life [5] of the laminate. The effects of these degradations emerge through phenomena such as shifts in the natural frequencies [6], mode localization [7], and variations in modal damping [8,9]. Although frictional contact, together with intrinsic material damping, contributes significantly to energy dissipation in debonded laminates, its isolated contribution to modal damping remains insufficiently quantified [10]. The magnitude of friction-induced dissipation is strongly influenced by contact-related parameters such as the coefficient of friction *COF*, the normal contact force, the effective contact area, and the relative slip between the surfaces [11–14]. These interfaces introduce nonlinear dynamic features, including superharmonic responses, that alter modal damping and distort expected vibration patterns, which may affect the reliability of vibration-based structural health monitoring (*VHM*) strategies [15]. Beyond these nonlinearities, interfacial friction may also lead to resonance shifts [16] and local heat generation, which further complicate dynamic modeling and vibration-based damage assessment of debonded laminates.

Classical models, such as those introduced in [11], quantify dissipation through cycle-based energy measures that condense frictional energy loss into equivalent modal damping ratios. While effective for estimating overall dissipation, these averaged metrics suppress amplitude-dependent and multi-frequency behaviors intrinsic to frictional contact. Subsequent experimental and theoretical studies have shown that structures dominated by frictional damping exhibit remarkable nonlinearities that cannot be captured adequately by equivalent damping

* Corresponding authors.
E-mail addresses: shabnam.kiasat@polito.it (S. Kiasat), matteo.filippi@polito.it (M. Filippi), a.salehzadeh-nobari@imperial.ac.uk (A.S. Nobari), erasmo.carrera@polito.it (E. Carrera).

https://doi.org/10.1016/j.ijnonlinmec.2026.105389
Received 16 February 2026; Received in revised form 15 May 2026; Accepted 16 May 2026
Available online 22 May 2026
0020-7462/© 2026 The Authors. Published by Elsevier Ltd. This is an open access article under the CC BY-NC-ND license (http://creativecommons.org/licenses/by-nc-nd/4.0/).

ratios [17]. More recent advances, including the nonlinear modal analyses developed by [18,19], further underscore the need for refined frameworks capable of resolving detailed frictional interactions within multi-harmonic responses. Motivated by these developments, this work proposes a hybrid time–frequency domain approach to capture superharmonic contributions by reconstructing friction-induced hysteresis loops at both the fundamental frequency and its higher-order superharmonics. This enables a more detailed assessment of interlaminar frictional dissipation and its influence on modal damping in debonded structures.

This work builds upon a previous experimental investigation by one of the authors [8], which examined variations in the modal parameters of delaminated composite structures with different delamination levels. That study yielded two key observations: first, the natural frequency exhibited limited sensitivity to small-scale delaminations and changed only slightly, even as the damage percentage increased, whereas modal damping showed significant variations, suggesting its potential as a more sensitive damage indicator (*DI*). Second, while natural frequencies demonstrated a monotonic trend with increasing delamination, modal damping exhibited non-monotonic behavior. This counterintuitive trend indicates that different energy dissipation mechanisms, such as the viscoelasticity of the resin or interfacial friction, may dominate specific vibration modes, and that delamination can affect the modal strain energy contribution. It should be noted that changes in modal strain energy due to delamination should also affect the structure's natural frequencies. However, the order of this change is small enough not to be captured in the natural frequency, and hence the natural frequency is insensitive to delamination. This is not the case in the modal damping coefficient, as the order of the magnitude of modal dissipation is small, and hence can be affected by small changes in the strain energy. To understand the non-monotonic behavior of modal damping, it is essential to examine how delamination affects modal damping for each dissipation mechanism separately, and hence this study. This enables identification of the dominant dissipation mechanism in each vibration mode. In a previous numerical study, the viscoelastic damping mechanism was investigated in a delaminated structure, without considering contact or friction between the separated layers [9]. The results showed that damping variations were most significant in regions of maximum strain for bending modes and maximum deformation for torsional modes. However, this approach could not fully explain the uneven variations in modal dissipation, which are likely driven by nonlinear effects such as frictional contact. Motivated by this limitation, the present study focuses on the numerical modeling of interfacial friction and its sensitivity to delamination. One objective is to provide a basis for investigating the interaction between material- and friction-related dissipation mechanisms, building upon the approach introduced in [20]. Accordingly, the present study examines friction-induced dissipation in the absence of other dissipation mechanisms, such as material damping. This assumption is not introduced to reproduce the modal damping of a specific test specimen, but to isolate the modal and spectral contributions of interfacial friction and to examine how these contributions are distributed between the fundamental response and the higher-order superharmonic components.

Beyond the experimental trends discussed above, further evidence from the literature shows that damaged or delaminated composites may exhibit nonlinear spectral features and higher-order harmonic components [21,22]. These observations support the need to interpret delamination-induced dissipation not only through linear stiffness reduction or a single equivalent damping parameter, but also through nonlinear modal and spectral contributions. Therefore, the present work does not aim to quantitatively reproduce a particular experiment. Rather, it is a mechanism-oriented numerical investigation that uses a controlled numerical setting to isolate and interpret the contribution of interfacial friction to modal dissipation in delaminated structures. This frictional mechanism is consistent with experimental evidence, but its direct isolation in real tests remains difficult, since several dissipation mechanisms may coexist, and the local frictional slip under vibration is not readily measurable. In particular, separating frictional slip from the accompanying elastic deformation at the interface is nontrivial, and substantial uncertainty may remain even when such a separation is attempted [14,23,24]. Within this scope, the objective is to provide a modal and time–frequency interpretation of friction-induced dissipation, using the experimental trends reported in the literature as qualitative reference points rather than as data for one-to-one validation.

The paper is structured as follows: Section 2 presents the numerical framework and contact modeling; Section 3 discusses the finite element *FE* model verification and *COF* sensitivity; Section 4 examines the dynamic response and parametric studies; and Section 5 summarizes the conclusions.

2. Numerical modeling framework

2.1. Modeling frictional contact

This section focuses on the contact behavior in laminate structures, addressing both normal and tangential interactions. Normal contact governs the interaction between debonded surfaces, while tangential contact accounts for frictional resistance to relative motion.

2.1.1. Normal contact

Normal contact at separated interfaces refers to the interaction between debonded layers perpendicular to their contact area [25]. The micromechanical approach (*MMA*) and the geometrical constraint approach (*GCA*) are two common approaches for modeling normal contact.

The *MMA* considers material behavior at the contact area, developing constitutive laws for microscale response and determining normal contact stresses based on applied loads and material properties. This approach describes contacts involving significant deformation or material interaction [26].

The *GCA* focuses on the geometry of contact, ensuring no overlap or penetration between bodies in the normal direction. It is particularly efficient for surface geometry-dominated contact with negligible deformation or material interaction [27].

A common formulation treats normal contact as a unilateral constraint problem, prioritizing correct contact behavior over specific material responses within the interface [26,28]. This approach does not require constitutive relations for the interface. Instead, the normal contact pressure is a reaction force resulting from the contact constraints. Referring to Fig. 1 for normal contact of 3D objects, the calculated distance determines the gap or penetration between the two bodies. The parameterization of boundary Γ^1 using convective coordinates is denoted by $\bar{\xi} = (\bar{\xi}^1, \bar{\xi}^2)$. For more detailed information on contact constraints, see [28–30].

Assuming local convexity of the contact boundary, the relation between each point x^2 on the contact boundary of body 2 (Γ^2) and its corresponding point $\bar{x}^1 = x^1(\bar{\xi})$ on the contact boundary of body 1 (Γ^1) is established by Eq. (1), which results from the minimum distance problem, see Fig. 1.

$$\hat{d}^1\left(\xi^1, \xi^2\right) = \left\| x^2 - \bar{x}^1 \right\| = \min_{x^1 \subseteq \Gamma^1} \left\| x^2 - \bar{x}^1 \right\| \tag{1}$$

The point $\bar{x}^1$ is determined by satisfying the necessary condition for the minimum of the distance function given by Eq. (1) and expressed by Eq. (2).

$$\frac{d}{d\xi^\alpha}\hat{d}^1\left(\xi^1, \xi^2\right) = \frac{x^2 - \bar{x}^1(\xi^1, \xi^2)}{\left\| x^2 - \bar{x}^1(\xi^1, \xi^2) \right\|} \cdot \hat{x}^1_{,\alpha} = 0 \tag{2}$$

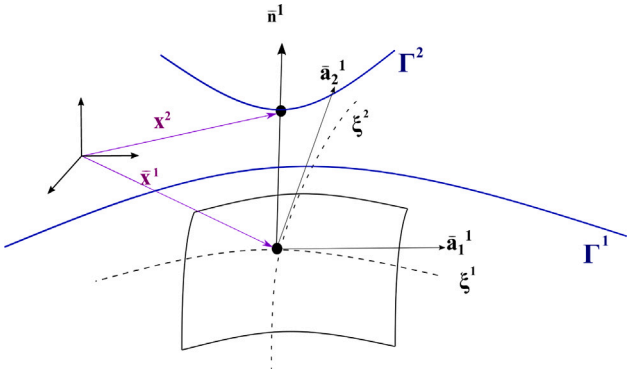

Fig. 1. Coordinate system and minimum distance for normal contact of 3D bodies.

To solve Eq. (2), the vector connecting the points $\mathbf{x}^2$ and $\bar{\mathbf{x}}^1$ must be orthogonal to the tangent plane at $\bar{\mathbf{x}}^1$. This orthogonality condition is expressed by Eq. (3).

$$-\mathbf{n}^1(\bar{\xi}^1,\bar{\xi}^2)\cdot\mathbf{a}_\alpha^1(\bar{\xi}^1,\bar{\xi}^2)=0 \tag{3}$$

where in Eq. (3), $\mathbf{a}_\alpha^1$ are the tangent vectors to the surface Γ^1 at the point $\bar{\mathbf{x}}^1$. This condition implies that $\bar{\mathbf{x}}^1=\mathbf{x}^1(\bar{\xi}^1,\bar{\xi}^2)$ is the orthogonal projection of the slave point $\mathbf{x}^2$ onto the master surface $\varphi_i^1(\Gamma_c^1)$. Here, a bar over a quantity denotes its evaluation at the minimal distance point $(\bar{\xi}^1,\bar{\xi}^2)$, representing the solution to Eq. (2).

The Eq. (4) gives the non-penetration condition for the contact between two objects, which can be expressed as $g_N\geq 0$, where g_N represents the normal component of the gap function. This condition ensures that no overlap or penetration occurs. Contact is established when $g_N=0$, at which point the normal stress corresponds to the contact pressure.

$$g_N=(x_2-\bar{x}_1)\cdot\bar{n}_1\geq 0 \tag{4}$$

According to the action-reaction principle, the reaction force (R_n) between contacting surfaces acts in the direction opposite to the surface normal. If the gap g between the surfaces is greater than zero, they are not in contact, and the reaction force is zero, following the Kuhn–Tucker condition [31]. This condition is defined by Eq. (5).

$$\begin{aligned} &R_n\leq 0\\ &g\cdot R_n=0\end{aligned} \tag{5}$$

To derive the normal contact formulation for non-penetration, we begin with the strong form of the equilibrium given by Eq. (6) [27].

$$\nabla\cdot\boldsymbol{\sigma}=\mathbf{b}\quad\text{in }\Omega \tag{6}$$

In Eq. (6), $\boldsymbol{\sigma}$ is the stress tensor, $\mathbf{b}$ is the body force vector, and Ω is the body domain. At the contact interface, the normal component of the stress vector, corresponding to the contact pressure, becomes non-zero upon contact. The Dirichlet (Γ_D) and Neumann (Γ_N) boundary conditions (BCs) (where $\partial\Omega=\Gamma_N\cup\Gamma_D$) for Eq. (6) are formulated as Eq. (7).

$$\begin{aligned} &\mathbf{u}=\mathbf{u}_g \qquad \text{on } \Gamma_D\\ &\boldsymbol{\sigma}\cdot\mathbf{n}=\mathbf{t}=\mathbf{t}_g \quad \text{on } \Gamma_N\end{aligned} \tag{7}$$

In Eq. (7)$\mathbf{u}$ is the displacement vector, $\mathbf{u}_g$ indicates the prescribed displacement, $\mathbf{n}$ shows the outward surface normal vector, and $\mathbf{t}$ is the traction vector with $\mathbf{t}_g$ being its prescribed value.

The weak form of the equilibrium Eq., including the contact contribution C_c, is expressed by Eq. (8).

$$\int_\Omega\boldsymbol{\sigma}:(\delta\mathbf{u}\otimes\nabla)\,d\Omega-\int_\Omega\mathbf{b}\cdot\delta\mathbf{u}\,d\Omega-\int_\Gamma\mathbf{t}\cdot\delta\mathbf{u}\,d\Gamma+C_c=0 \tag{8}$$

Let ε denote the penalty parameter enforcing the contact constraint. The potential energy of the contact zone (Π_c) is given by Eq. (9).

$$\Pi_c=\frac{1}{2}\int_{\Gamma_c}\varepsilon g^2\,d\Gamma \tag{9}$$

Note that Eq. (9) specifically applies to frictionless contact scenarios. In the presence of friction, energy dissipation introduces path dependency, complicating the potential energy formulation. By combining Eqs. (8) and (9) through the penalty method, the weak form is described by Eq. (10).

$$\int_\Omega\boldsymbol{\sigma}:(\delta\mathbf{u}\otimes\nabla)\,d\Omega-\int_\Omega\mathbf{b}\cdot\delta\mathbf{u}\,d\Omega-\int_\Gamma\mathbf{t}\cdot\delta\mathbf{u}\,d\Gamma-\int_{\Gamma_c}\varepsilon g\,d\Gamma=0 \tag{10}$$

2.1.2. Tangential contact

In mechanical contact mechanics, tangential behavior is governed by either a geometric constraint approach or a frictional constitutive law [32]. Two primary scenarios are analyzed: sticking and sliding [33]. Under sticking conditions, where no relative tangential motion occurs between contacting surfaces, a geometric constraint enforces equal tangential displacements at the interface, effectively preventing tangential movement. Conversely, a constitutive law dependent on the interface and material properties describes frictional forces based on the normal contact force, relative tangential velocity, and slip distance during sliding conditions. Accurate modeling requires careful consideration of the stick condition, characterized by zero relative tangential displacements and velocity [34]. Let g_T represent the relative tangential displacement; the stick condition corresponds to zero relative tangential displacement and velocity ($\dot{g}_T$), Eq. (11).

$$g_T=0\quad\leftrightarrow\quad\dot{g}_T=0 \tag{11}$$

Enforcing the stick condition at the contact interface requires suitable constitutive relations to govern tangential contact behavior during stick–slip motion. A penalty term, introduced to enforce the constraint, modifies Eq. (9) and modifies the potential energy expression, which is represented by Eq. (12).

$$\Pi_c^P=\frac{1}{2}\int_{\Gamma_C}\left(\varepsilon_N(\bar{g}_N)^2+\varepsilon_T g_T\cdot g_T\right)dA,\quad \varepsilon_N,\varepsilon_T>0 \tag{12}$$

where in Eq. (12)ε_N and ε_T are the penalty parameters. The penalty term Π_c^P is added only for active constraints, defined by the penetration function g_N, and formulated for normal and tangential contact. For pure stick in the contact interface, the variation of Eq. (12) can be written as Eq. (13).

$$C_c^P=\int_{\Gamma_c}\left(\varepsilon_N\bar{g}_N\,\delta\bar{g}_N+\varepsilon_T g_T\cdot\delta g_T\right)dA,\quad \varepsilon_N,\varepsilon_T>0 \tag{13}$$

The tangential component applies only under stick conditions. The slip condition is described by Eq. (14).

$$C_c^{slip}=\int_{\Gamma_c}\left(\varepsilon_N\bar{g}_N\,\delta\bar{g}_N+t_T\cdot\delta\bar{g}_T\right)dA,\quad \varepsilon_N>0 \tag{14}$$

In frictional sliding, the tangential stress vector ($\boldsymbol{\tau}_T$) is determined by a friction constitutive law (e.g., Coulomb friction, as used in this study). Coulomb friction governs relative motion between contacting surfaces [27], stating that relative motion occurs only when the frictional shear stress (τ) exceeds a critical threshold, as formulated by Eq. (15).

$$\boldsymbol{\tau}_T=-\mu\left|p_N\frac{\dot{g}_T}{\|\dot{g}_T\|}\right|\quad\text{if}\quad\|\boldsymbol{\tau}_T\|\geq\mu|p_N| \tag{15}$$

In Eq. (15), μ represents the sliding coefficient of friction (COF), p_N is the normal pressure, and $\dot{g}_T$ shows the sliding velocity. Although μ is typically constant in the classical Coulomb law, it can vary due to surface roughness, sliding velocity, pressure, and temperature. Hence, the variable COF in Coulomb's law, denoted as $\mu=\mu(\dot{g}_T,F_N,\theta)$, can be expressed by Eq. (16).

$$\mu(\dot{g}_T)=\mu_D+(\mu_S-\mu_D)\,e^{-d_C\|\dot{g}_T\|} \tag{16}$$

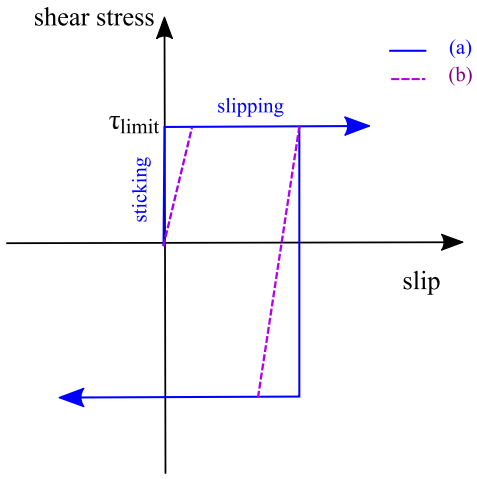

Fig. 2. Ideal (a) and penalty (b) stick–slip behavior [20].

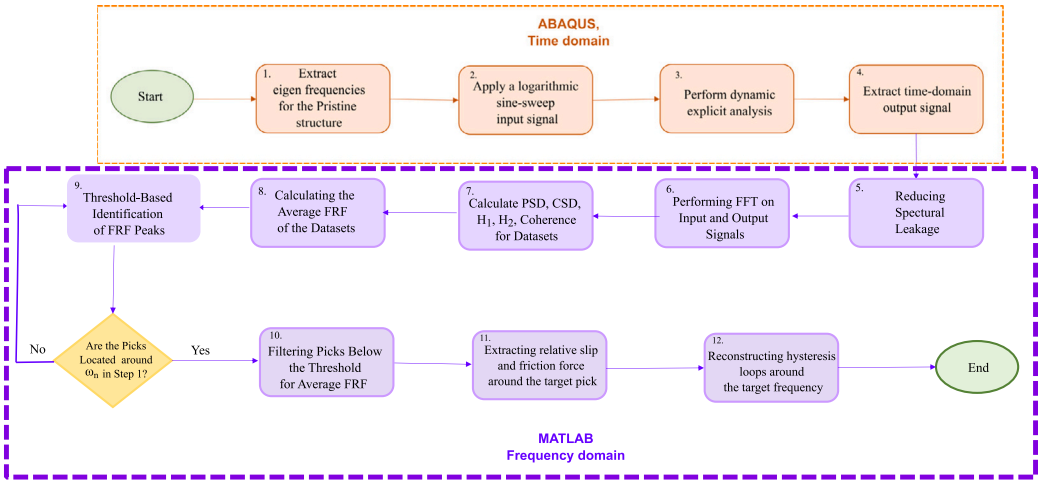

Fig. 3. Procedure for time and frequency domain analysis [20].

The static *COF*, μ_S, denotes friction at zero relative sliding velocity, while μ_D represents the value at intermediate sliding velocity. The decay coefficient d_C governs how friction diminishes with increasing relative velocity.

Even when a friction model indicates stick behavior, incremental slip can occur due to elastic displacements induced by surface roughness [35], leading to slight displacements between contacting surfaces. To address elastic slip, the conventional Coulomb friction model (Fig. 2(a)) is modified (Fig. 2(b)) [27].

In *ABAQUS*, elastic slip may be prescribed either as an absolute displacement or as a fraction of the characteristic surface dimension. Here, the latter definition was adopted.

2.2. Time and frequency domain analysis

The frequency response function (*FRF*) is obtained by transforming time-domain data into the frequency domain via the fast Fourier transform (*FFT*). Frequency-domain analysis begins with windowing the signals to reduce spectral leakage, after which the data are converted to reveal dominant frequencies (Fig. 3).

The power spectral density (*PSD*) is calculated by Eq. (17).

$$PSD_{XX} = \frac{\mathrm{FFT}(X) \cdot \mathrm{FFT}(X)^*}{f_{\mathrm{sampling}} \cdot N} \tag{17}$$

The cross spectral density (*CSD*) quantifies the correlation between input and output signals, as shown in Eq. (18).

$$CSD_{XF} = \frac{\mathrm{FFT}(X) \cdot \mathrm{FFT}(F)^*}{f_{\mathrm{sampling}} \cdot N} \tag{18}$$

The FRF_1 is calculated by Eq. (19).

$$FRF_1 = \frac{CSD_{XF}}{PSD_{FF}} \tag{19}$$

Alternatively, the FRF_2 is formulated as Eq. (20).

$$FRF_2 = \frac{PSD_{XX}}{CSD_{XF}} \tag{20}$$

Here, X and F denote the response and excitation spectra obtained via *FFT*, respectively, while f_{sampling} represents the sampling frequency and N the number of *FFT* points. Eq. (20) is therefore used to improve estimation near resonant regions. In this study, the analyzed frequency range extends up to 5000 Hz, and $\Delta t_{\mathrm{sampling}}$ is defined according to the frequency bandwidth of interest. In contrast, $\Delta t_{\mathrm{dynamic}}$ denotes the time increment of the nonlinear explicit solver and is significantly smaller, requiring signal resampling during post-processing. Multiple downsampled datasets were generated (see Fig. 4) to compute averaged *FRF* that reduces numerical fluctuations and spectral inconsistencies. Further details can be found in [36–38].

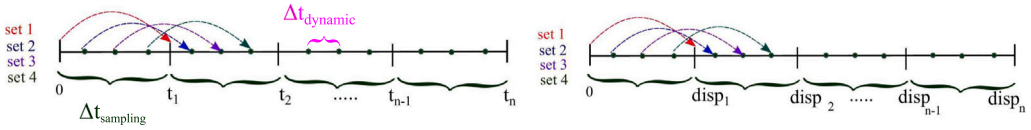

Fig. 4. Downsampling of data sets for computing the average *FRF*.

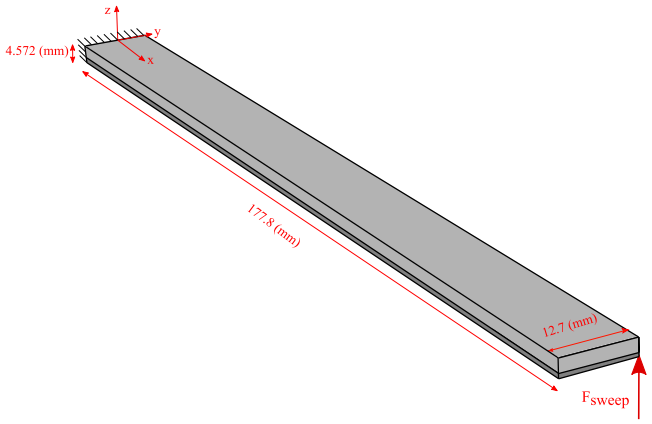

Fig. 5. Schematic of the two-layered beam along with *BC*s and loading location.

3. Model verification and the COF sensitivity analysis

In this section, we first verify the accuracy of the FE model and the computational efficiency of the workflow illustrated in Fig. 3. Subsequently, we investigate how variations in COF within a specified range affect the damping behavior of the debonded structure.

3.1. Model setup and verification

A two-layered model of a purely elastic beam with thicknesses of t and $2t$ is considered, with the left end rigidly clamped and the right end free, as shown in Fig. 5. This configuration enables the investigation of interfacial friction despite the isotropic material behavior. The material properties are defined as Young's modulus $E = 69$ GPa, density $\rho = 2766$ kg/m^3, and Poisson's ratio $\nu = 0.3$.

In this study, a logarithmic sine-sweep excitation with an amplitude of 1(N) is applied, with the instantaneous frequency $f(t)$ defined by Eq. (21).

$$f(t) = \frac{f_i\left(-1+2^{Rt}\right)}{R\ln(2)} \tag{21}$$

where in Eq. (21), f_i is the starting frequency (Hz), R shows the sweep rate (octave/min), and t is time. The value of R is determined by dividing the total number of octaves (N_{octaves}) by the sweep duration, as expressed in Eq. (22), where f_o represents the ending frequency (Hz).

$$N_{octaves} = \frac{\ln\left(\frac{f_o}{f_i}\right)}{\ln(2)} \tag{22}$$

Interested readers are referred to [39–42] for more details.

Fig. 6 illustrates the first three bending modes (B_1, B_2, B_3) and the first torsional mode (T_1) of the pristine structure, along with their natural frequencies. We performed a convergence analysis by refining the FE mesh. The selected model is sufficiently accurate while maintaining an affordable computational cost. The peaks in the *FRF* depicted in Fig. 7 correspond closely to the identified natural frequencies, thereby verifying the algorithm presented in Fig. 3.

We conducted a two-step sensitivity analysis to ensure numerical stability and physical accuracy. First, for the pristine structure, we selected the mesh that best matched the fundamental mode by comparing peak frequencies from the FFT-based FRF with natural frequencies obtained from eigenvalue modal analysis. Once the stable mesh domain was identified, energy-based criteria were used to evaluate the debonded configurations. Meshes showing smooth and physically consistent kinetic and strain energy evolution were retained for all simulations.

Second, we used the central difference integration scheme of $ABAQUS$ Explicit for time step sensitivity. Fixed time steps introduced instability, so we adopted the $ABAQUS$'s automatic time increment control, which dynamically adjusts the time step based on a stability criterion. To validate this approach, we again analyzed the frequency response of the pristine structure under sine-sweep excitation. The resulting FRF showed distinct peaks closely matching theoretical modal frequencies, confirming that the automatically selected time steps were sufficiently small to capture the system's dynamic behavior.

3.2. Sensitivity analysis of the COF

Next, we examine the effect of the *COF* on the dissipative behavior of the debonded structure (see Fig. 5). A 20% interface debonding is introduced at the interface between layers, configured transversely (Fig. 8(a)). The *COF* values are derived from data in [43].

The Average Frictional Dissipated Power ($AFDP$) is calculated by dividing the accumulated Frictional Dissipated Energy (FDE), obtained at the end of the total analysis duration, by the total analysis time, as shown in Eq. (23).

$$AFDP = \frac{E_f(T)}{T} \tag{23}$$

In Eq. (23), $E_f(T)$ represents the $AFDE$ at the final time, while T denotes the total analysis time.

A two-second dynamic explicit analysis was undertaken to determine the *AFDP* for various *COF* values (Fig. 8). Since the effective coefficient of friction depends on local interface conditions and was not calibrated here against a specific experiment, the selected *COF* values were used to span representative friction regimes in the numerical study, ranging from relatively low tangential resistance to higher-friction conditions associated with partial slip or near-sticking behavior. As shown in Fig. 8(b), the computed *AFDP* varies only moderately across the explored range and exhibits a local minimum around ($\mu = 1.1$). This value was therefore selected as the reference case for the subsequent analyses.

4. Nonlinear dynamic behavior and parametric analyses

This section explores the influence of superharmonic presence on the response of nonlinear vibrations in debonded structures, specifically those affected by debonding-induced frictional contact. Initially, we calculate the pseudo-modal damping coefficient through superharmonic responses and their effects on damping behavior (Section 4.1). Next, we conduct a parametric analysis to understand the effects of various debonding parameters on the nonlinear dynamic response of the debonded structure. This includes an examination of debonding patterns (Sections Section 4.2.1), their distances from the neutral axis (Sections Section 4.2.2), and variations in their size (Section 4.2.3).

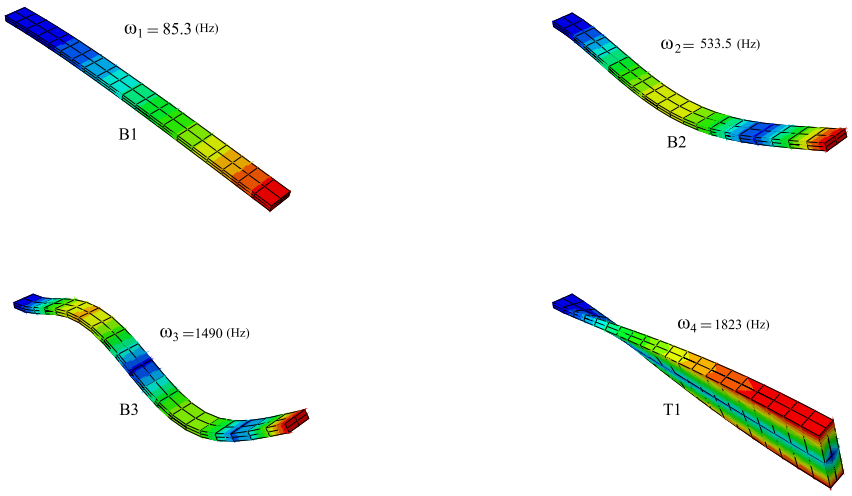

Fig. 6. Mode shapes and the natural frequencies of the first three bending modes and the first torsion mode of the pristine structure.

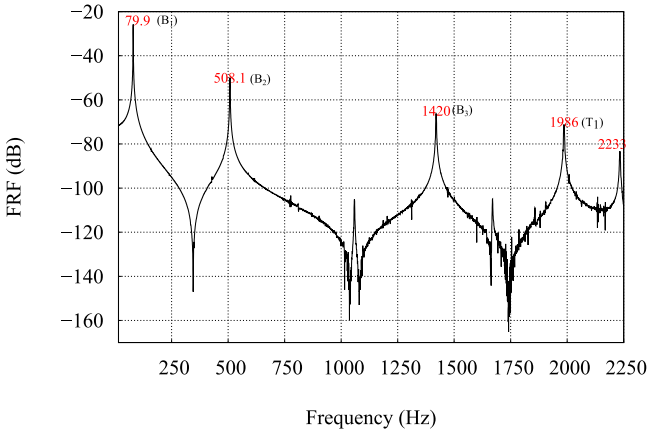

Fig. 7. Point-FRF of the pristine structure obtained from the temporal history using the algorithm illustrated in Fig. 3.

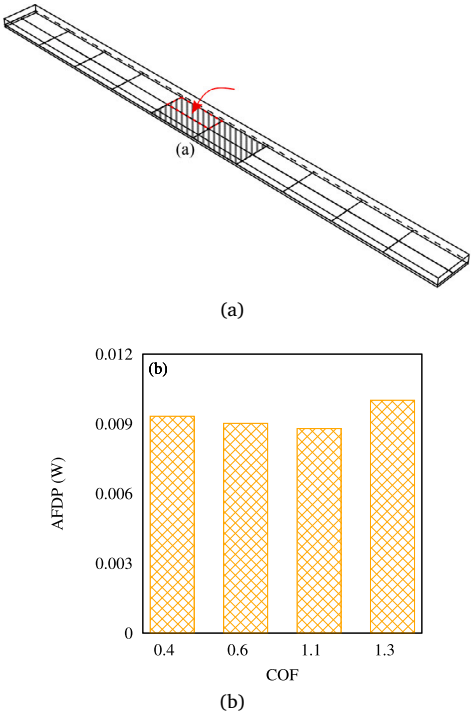

Fig. 8. (a) 20% debonding of the layers' interface, indicated by hatching. (b) Average Frictional Dissipated Power ($AFDP$) across the COF range, computed for the debonded region in (a).

4.1. Pseudo-modal damping coefficient and superharmonic responses

Nonlinearities arising from various sources, such as large deformations or frictional contact, give rise to vibrational phenomena absent in linear systems, including amplitude-dependent resonance and nonlinear damping characteristics [42,44,45]. In the present study, the nonlinear behavior mainly arises from frictional interactions associated with interfacial debonding, characterized by intermittent contact and stick–slip transitions that generate superharmonic components in the response. These superharmonics correspond to frequency components at integer multiples of the fundamental excitation frequency and arise from intrinsic nonlinear interactions within the structure rather than from external forcing. In a harmonically excited nonlinear system, the steady-state response simultaneously contains the fundamental and its superharmonics, reflecting the system's intrinsic nonlinear dynamics rather than resulting from modal superposition or independent harmonic contributions. Under certain excitation conditions, the amplitude of superharmonic responses can become comparable to, or even exceed, that of the fundamental harmonic, producing highly unpredictable patterns of energy dissipation, significantly altering the dynamic stability of the structure [46–48]. Therefore, superharmonics can indicate structural damage.

The analysis of superharmonic resonances is particularly critical for developing effective damage-detection strategies and for understanding the complex vibratory response of debonded structures [49]. Importantly, the emergence of these higher-order spectral components, as predicted by our framework, is well-supported by previous experimental observations [21,22].

To quantify the FDE in the modal frame, we introduce the dimensionless pseudo-modal damping coefficient, η_n, defined as Eq. (24).

$$\eta_n = \frac{S_{\text{hysteresis},n}}{SE^{(1)}_{\text{RMS}}} \tag{24}$$

Fig. 9 summarizes the procedure used to derive η_n from the time histories of interfacial slip and friction force obtained from the explicit FE analysis.

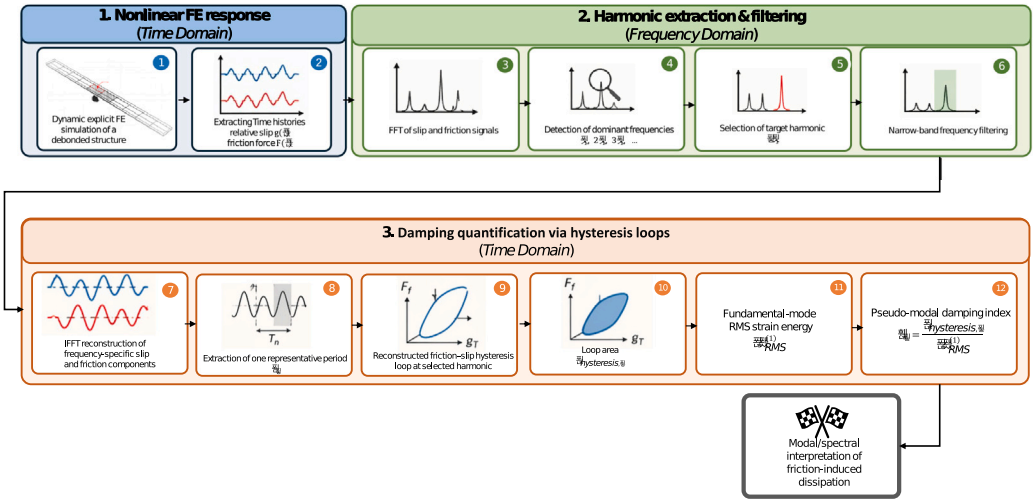

Fig. 9. Flowchart of the proposed hybrid time–frequency post-processing framework used to derive the pseudo-modal dissipation index from the time histories of interfacial slip and friction force obtained from the explicit FE analysis.

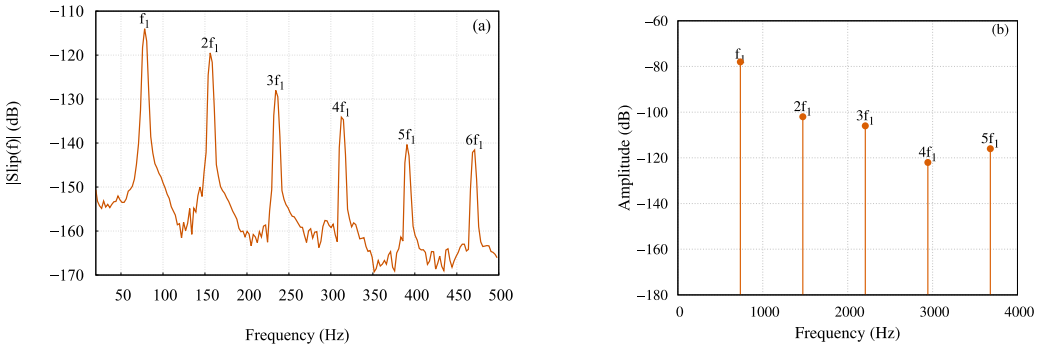

Fig. 10. Comparison of higher-order harmonic components: (a) numerical FFT spectrum of the frictional slip in the debonded region highlighted in Fig. 8(a); (b) approximate harmonic peak amplitudes replotted from the damaged composite response reported by Klepka et al. [21].

The pseudo-modal damping coefficient, η_n, is evaluated for the nth superharmonic, with $n = 1$–6. Here, $n = 1$ corresponds to the fundamental mode, while $n = 2$–6 represent the first five superharmonics. $S_{\text{hysteresis},n}$ denotes the area enclosed by the hysteresis loop associated with the nth superharmonic. $SE^{(1)}_{\text{RMS}}$ denotes the band-limited root mean square (*RMS*) strain energy of the fundamental mode, extracted from the power spectral density (*PSD*) of the strain energy time history. It is computed as Eq. (25).

$$SE^{(1)}_{\text{RMS}} = \frac{1}{\sqrt{2}}\sqrt{\int_{0.9f_1}^{1.1f_1} PSD_{SE}(f)\,df} \tag{25}$$

where PSD stands for Power Spectral Density, f_1 is the first natural frequency, and the integration limits define a ±10% frequency band around the fundamental mode. This quantity represents the effective (RMS) strain energy content concentrated within this modal frequency band.

Fig. 10(a) shows the slip spectrum for the debonded region highlighted by the arrow in Fig. 8(a). Due to the nonlinear nature of frictional contact, the response is not confined to the fundamental frequency but includes significant higher-order harmonic components [50,51]. For qualitative comparison, Fig. 10(b) reports approximate harmonic peak amplitudes replotted from the damaged-plate response spectrum reported in Ref. [21], obtained under excitation at the eighth vibration mode. In that study, the in-plane motion of delaminated plies was related to frictional interaction, including micro-slip at low excitation levels and stick–slip motion at higher levels, which can lead to harmonic generation and hysteretic dissipation. The experimental spectrum is used here as representative evidence that damaged composite interfaces can exhibit nonlinear harmonic content, while the present numerical framework examines this response by isolating the effect of interfacial frictional contact.

Figs. 11–12 display the hysteresis loops and their correspondence η_n values for the damaged structure shown in Fig. 8(a) as a case study. As evident from Fig. 11, with increasing *COF*, the interface progressively evolves from gross slip toward partial-slip or sticking conditions, which alters the hysteresis loops and redistributes dissipation across the spectrum [52]. Consequently, the dependence of η_n on *COF* is non-monotonic, and a minimum in the overall frictional dissipation may coexist with relatively high pseudo-modal indices in the fundamental and first superharmonic components, as shown in Figs. 8(b)–12. This behavior indicates that dissipation remains primarily governed by the low-order components, while higher-order superharmonics are increasingly suppressed [53].

4.2. A parametric study of debonding characteristics

4.2.1. Debonding pattern effect

This part compares the dynamic response of beams with 20% longitudinal and transverse debonding patterns (Fig. 13). Fig. 14 displays the temporal response for these cases, corresponding to the excitation node shown in Fig. 5. The four subplots illustrate magnified time intervals within the 2-second analysis.

In Fig. 14(a), a transient response is observed, where the initial oscillations gradually decay as the system approaches a steady-state

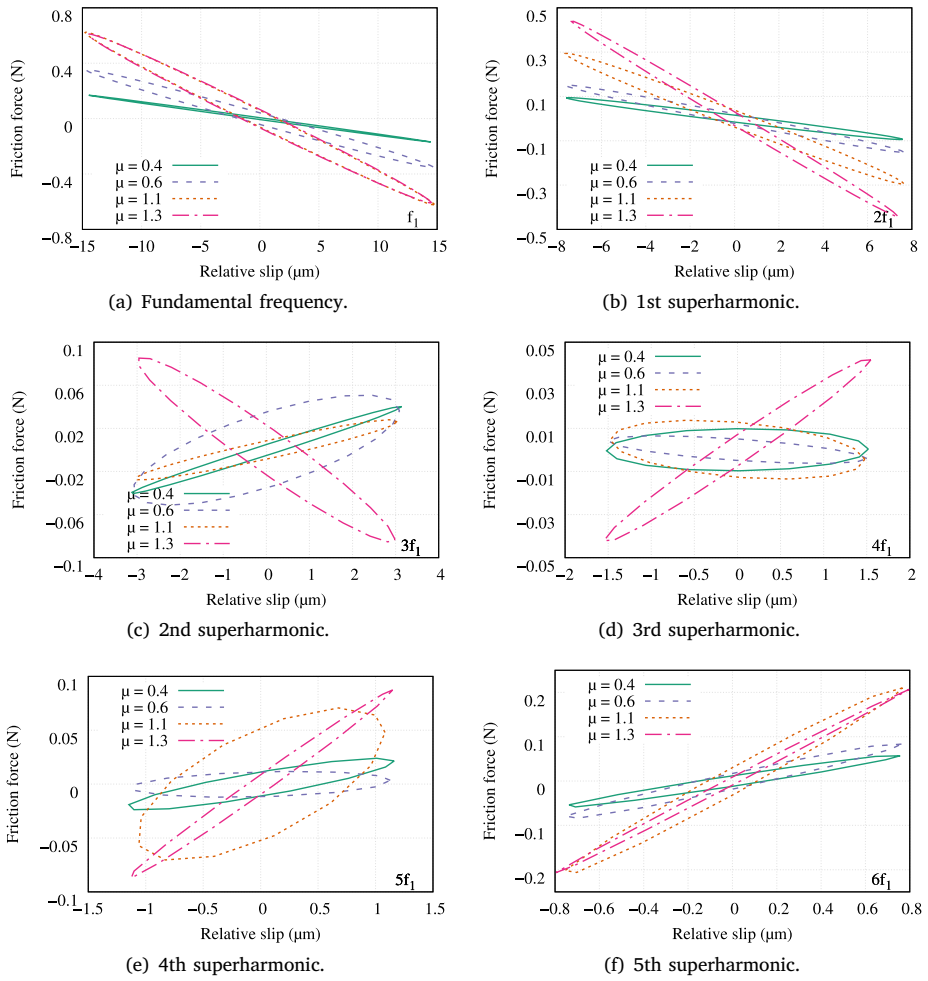

(a) Fundamental frequency. (b) 1st superharmonic.

(c) 2nd superharmonic. (d) 3rd superharmonic.

(e) 4th superharmonic. (f) 5th superharmonic.

Fig. 11. Slip-friction hysteresis loops of the arrowed part of the debonded region (hatched area in Fig. 8(a)). (a) First-mode frequency (f_1); (b–f) first five harmonics ($2f_1$–$6f_1$).

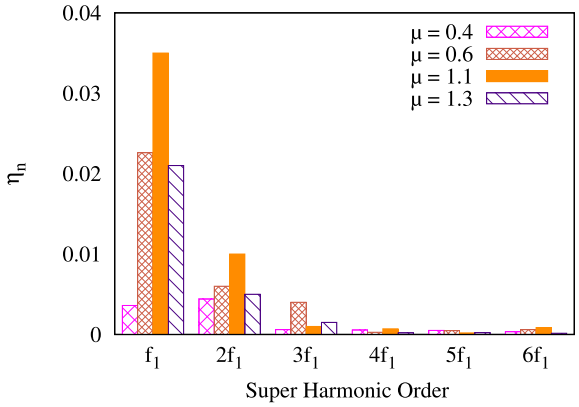

Fig. 12. Distribution of the energy-based pseudo-modal dissipation index (η_n), computed for the fundamental mode ($n = 1$) and its first five superharmonic responses ($n = 2-6$), for various values of the *COF*.

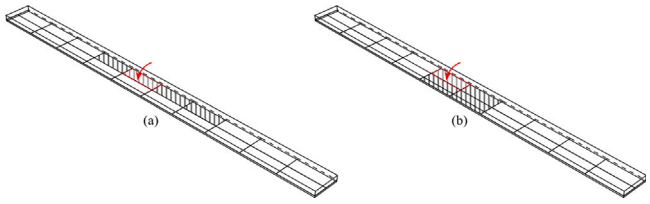

Fig. 13. 20% debonding of the layers' interface, indicated by hatching: (a) along the length, and (b) across the width of the interface.

regime; the case study with transverse debonding exhibits slightly larger amplitudes. This increase in amplitude is primarily due to the reduced effective stiffness in the transversely damaged configuration, in which the layers are fully separated within the debonded region, thereby reducing structural constraint. In Fig. 14(b), a significant amplitude jump occurs when the excitation frequency intersects the first natural frequency of the structure, corresponding to resonance crossing. This amplification is more remarkable for the transverse case, suggesting a higher sensitivity to dynamic excitation due to its lower local stiffness. Furthermore, Fig. 14(d) highlights waveform distortions associated with higher-order vibration modes and nonlinear contact effects. The transversely-damaged case shows stronger nonlinear characteristics, while the longitudinally damaged case behaves more similarly to the pristine structure.

Fig. 15 shows the point-FRF plot for damaged structures with longitudinal and transverse interface damage.

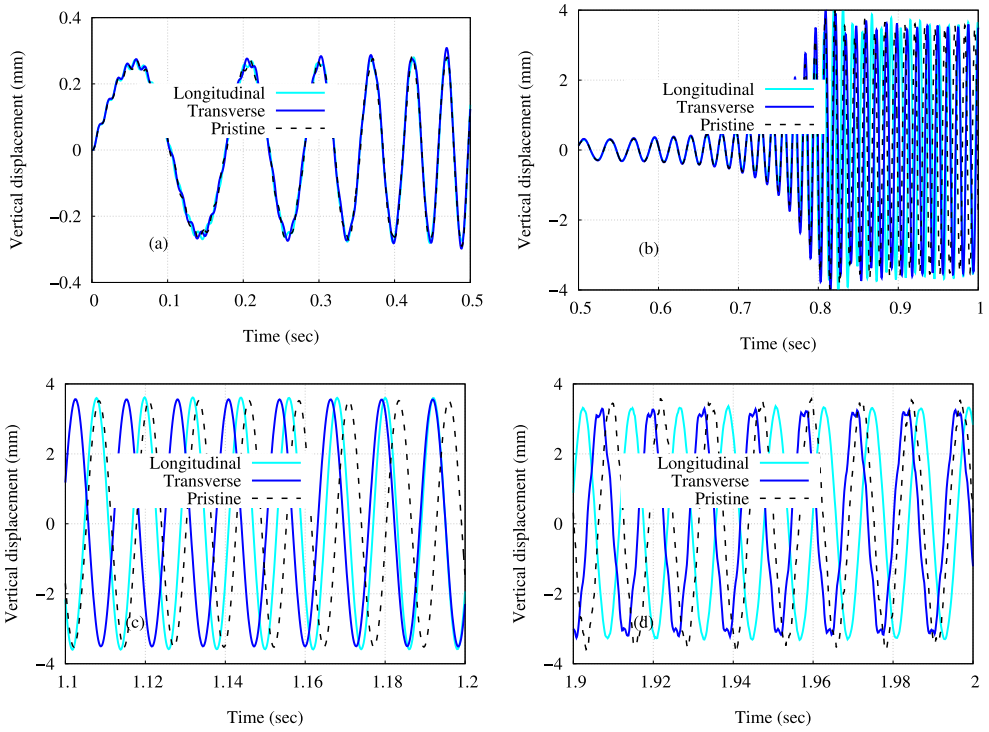

Fig. 14. Temporal history of the vertical displacement at the loading point for structures with 20% debonding of the interfaces: longitudinal (Fig. 13(a)) and transverse (Fig. 13(b)).

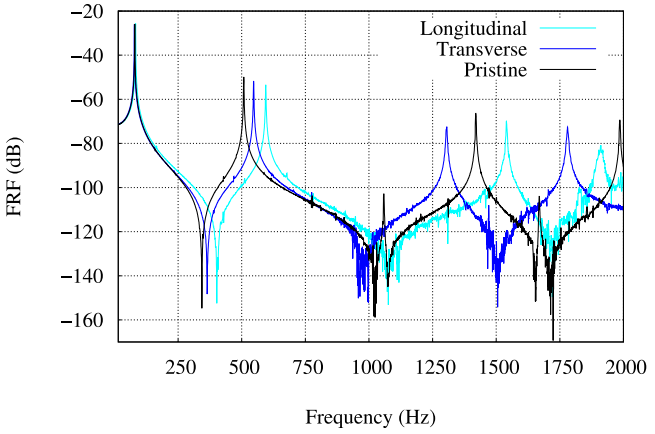

Fig. 15. Point–*FRF* of the structure with 20% interface debonding: longitudinal (Fig. 13(a)) and transverse (Fig. 13(b)).

The results in Fig. 15 indicate that not all vibration modes exhibit the same sensitivity to interface debonding. While the first bending mode (B_1) remains almost unaffected and the second bending mode (B_2) shows only limited sensitivity, the third bending mode (B_3) and the first torsional mode (T_1) emerge as the most informative for damage characterization. For these modes, the damage orientation (longitudinal or transverse) is clearly reflected in the frequency response, and a distinct separation among the pristine, transversely, and longitudinally damaged structures is observed. In particular, the strong sensitivity of B_3 indicates a significant interaction between the debonded region and the high-strain zones of the corresponding mode shape [9]. Similarly, T_1 is physically highly relevant, as it is directly governed by the interlayer shear coupling. Since interface debonding primarily degrades this shear transfer mechanism, the torsional response is strongly affected.

Although the influence of damage orientation can be identified in the responses of certain vibration modes, the modal damping parameter provides a more physically meaningful basis for interpreting the damage-induced changes [10].

To further examine the effect of interfacial damage on the structural energy response, the normalized strain energy (*NSE*) is evaluated by comparing the damaged configurations with the pristine structure (see Eq. (26)). The *NSE* is defined as the ratio of the cumulative strain energy of the damaged structure to that of the pristine one.

$$\mathrm{NSE} = \frac{\int_0^T \mathrm{SE}_{\mathrm{damaged}}(t)\,\mathrm{d}t}{\int_0^T \mathrm{SE}_{\mathrm{pristine}}(t)\,\mathrm{d}t} \tag{26}$$

Fig. 16 presents the *FDE* distribution within the structure over the entire analysis. Subplot (a) highlights the initial stage and the stick–slip transition. In addition, Fig. 17(a)–(b) reports the corresponding η_n and *NSE* values for the damaged configurations illustrated in Fig. 13.

Fig. 16 shows that the transversely debonded case activates sliding earlier and exhibits a steeper growth of *FDE*, indicating stronger frictional interactions. In contrast, when the delamination is aligned with the dominant vibration mode (longitudinally damaged case), interfacial slip is less effectively triggered, leading to lower overall dissipation [54]. Although the transverse configuration yields a larger total *FDE*, the longitudinally debonded structure exhibits higher dissipation when the first bending mode is excited (around $t \approx 0.75$ s).

These trends are also evident in the distributions of η_n and the NSE in Fig. 17(a)–(b). In the longitudinally damaged case, the debonded interface lies in a region of higher fundamental-mode deformation, so excitation of the first mode more effectively promotes interfacial slip and frictional dissipation. By contrast, in the transverse configuration, dissipation becomes dominant at higher frequencies. The higher NSE observed in the transverse case may reflect changes in the interfacial load-transfer characteristics and the corresponding deformation patterns. These effects could lead to increased local strain concentrations and elastic energy storage near the debonded zone. This qualitative

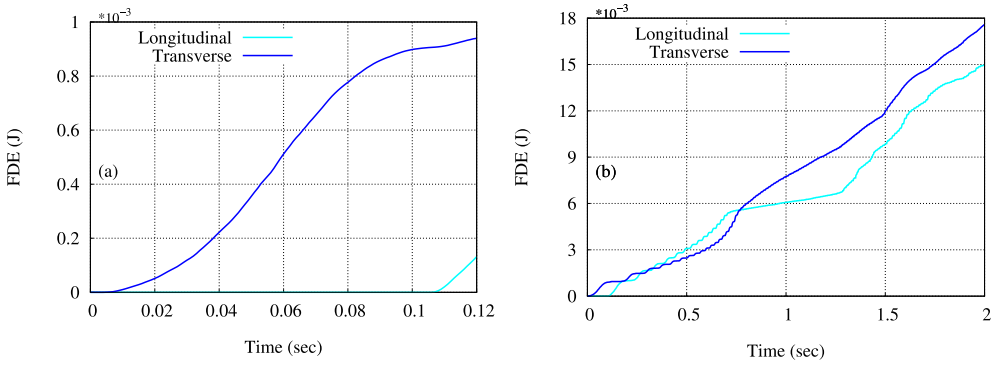

Fig. 16. Temporal *FDE* of the entire structure for 20% interface debonding: longitudinal (Fig. 13(a)) and transverse (Fig. 13(b)).

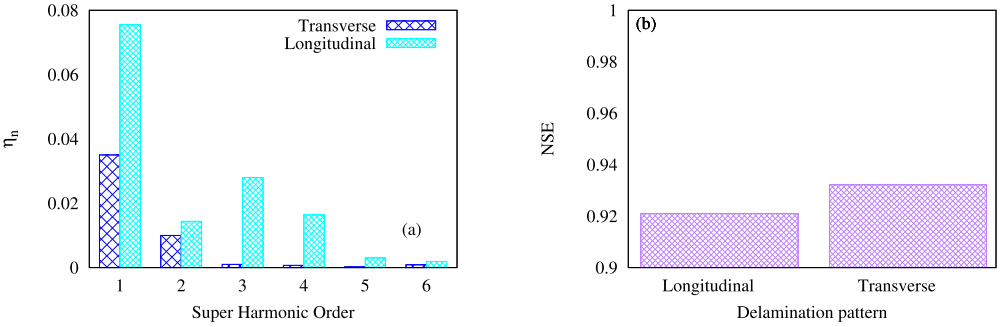

Fig. 17. (a) Distribution of the energy-based pseudo-modal dissipation index (η_n), computed for the fundamental mode ($n = 1$) and its first five superharmonic responses ($n = 2-6$), (b) *NSE* for structures with 20% interface debonding: longitudinal (Fig. 13(a)) and transverse (Fig. 13(b)).

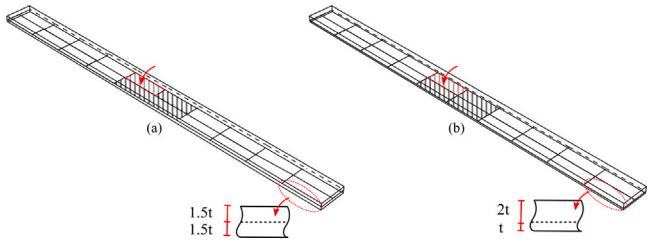

Fig. 18. 20% transverse debonding of the layers' interface, indicated by hatching: (a) symmetric and (b) asymmetric with respect to the neutral axis.

trend is consistent with previous experimental observations showing that the dynamic response of delaminated composite structures depends sensitively on the damage orientation, location, and the associated local stiffness redistribution [22,55].

4.2.2. Determination distance relative to neutral axis

This section examines the influence of the interface debonding distance from the neutral axis on the dynamic characteristics of the debonded beam. The study encompasses symmetric and asymmetric configurations, as depicted in Fig. 18, where the interface is located at the mid-thickness $(1.5t, 1.5t)$ for the symmetric case (Fig. 18(a)) and at $(t, 2t)$ for the asymmetric case (Fig. 18(b)).

Fig. 19 shows the temporal response of the symmetric and asymmetric delaminated configurations. The four subplots show magnified portions of the 2 (s) time history. It is observed from Fig. 19 that in the symmetric case study, the delamination is located close to the neutral axis, resulting in weaker bending–extension coupling and a more balanced stress field [56]. Consequently, the response remains more regular and closer to the pristine behavior. In contrast, in the asymmetric configuration, the offset of the delamination from the neutral axis enhances bending–extension coupling, promoting stronger energy transfer into the vibration modes. This results in a more nonlinear response, larger vibration amplitudes, and greater sensitivity to dynamic excitation.

Fig. 20 shows the point-FRF for damaged structures with symmetric and asymmetric configurations. B_1 is less affected, as the debonding occurs near a weakly deformed region of the mode shape. Similarly, B_2 shows limited sensitivity in the asymmetric configuration for the same reason. In contrast, B_3 and T_1 exhibit clearer frequency shifts, since the debonded region is located close to high-strain and high-deformation zones of the corresponding mode shapes, consistent with our previous findings [9]. In these modes, symmetric debonding leads to a larger reduction in effective stiffness than asymmetric debonding, as both sides of the interface are equally affected. This results in a more global degradation of the cross-section and a stronger weakening of the interlaminar coupling. Consequently, a larger drop in natural frequencies is observed. Fig. 21 presents the FDE throughout the analysis. Fig. 21(a) highlights the early moments and the transition from stick to slip. Fig. 22(a)–(b) indicates the η_n and *NSE* values for the damaged structures shown in Fig. 18.

Fig. 21 shows that the symmetric configuration activates sliding earlier, whereas the asymmetric case accumulates a larger total *FDE* at later times. This delayed yet stronger dissipation in the asymmetric configuration is associated with the bending–extension coupling induced by the offset delamination, which enhances contact asymmetry and promotes more intense stick–slip interactions [56].

This change in dissipation mechanism is also evident in Fig. 22. In the asymmetric configuration, bending–extension coupling drives frictional slip directly through the fundamental bending response, yielding a dominant contribution of the first natural mode. By contrast, in the symmetric case, frictional dissipation is activated more gradually through nonlinear interactions, leading to a redistribution of energy toward higher superharmonics. Hence, even though the total dissipation becomes comparable near the first resonance, the asymmetric configuration is characterized by modal-dominated dissipation, whereas the

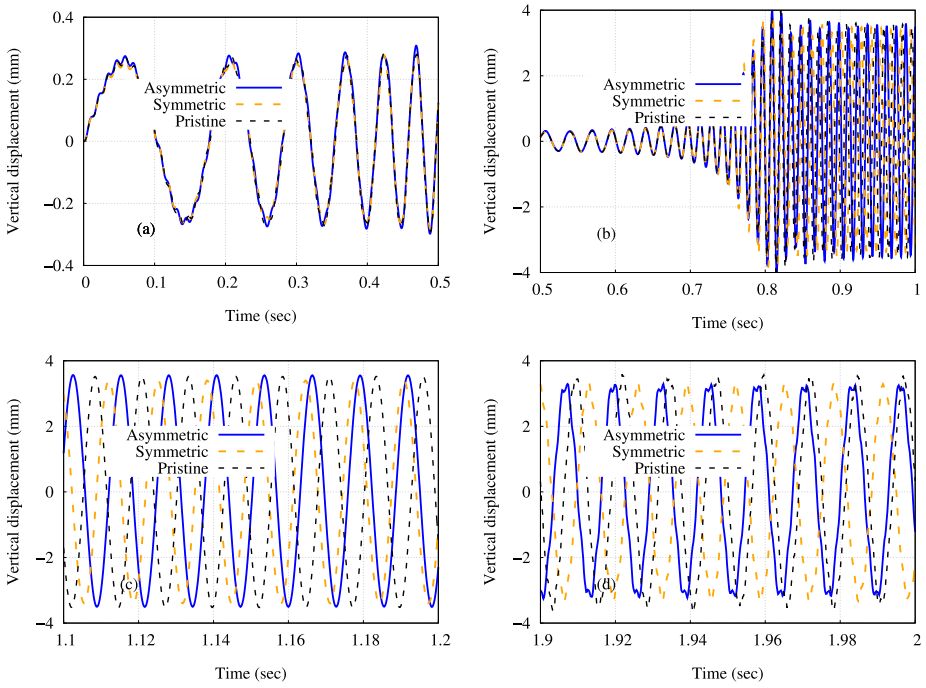

Fig. 19. Temporal history of the vertical displacement at the loading point for structures with 20% debonding of the interfaces: symmetric (Fig. 18(a)) and asymmetric (Fig. 18(b)) configurations.

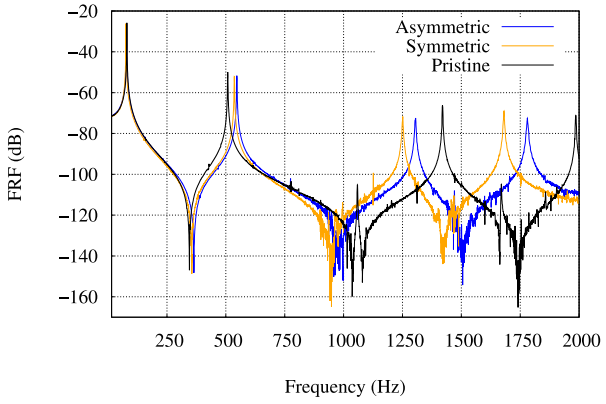

Fig. 20. Point *FRF* of the structure with 20% interface: symmetric (Fig. 18(a)) and asymmetric (Fig. 18(b)) configurations.

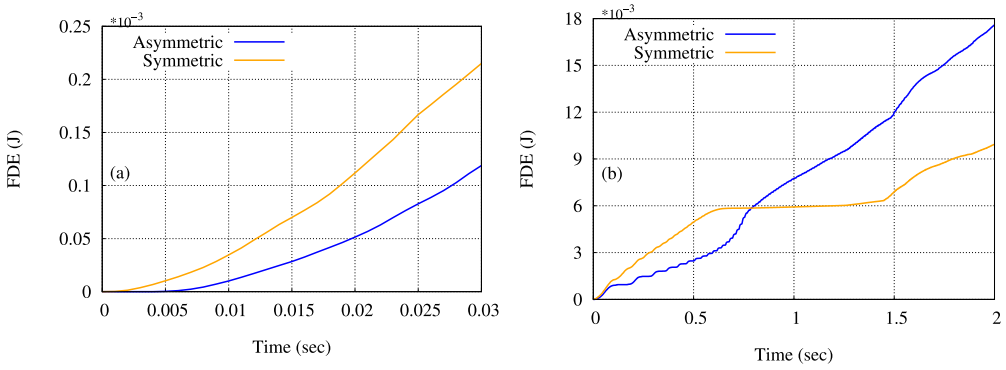

Fig. 21. Temporal *FDE* of the entire structure for 20% interface debonding: symmetric (Fig. 18(a)) and asymmetric (Fig. 18(b)) configurations.

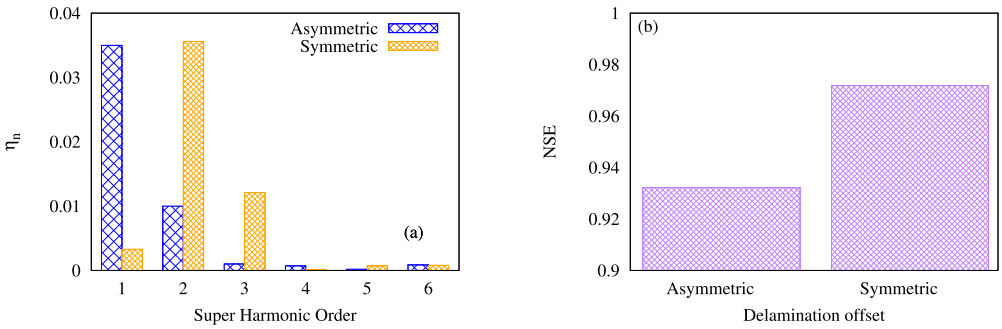

Fig. 22. (a) Distribution of the energy-based pseudo-modal dissipation index (η_n), computed for the fundamental mode ($n = 1$) and its first five superharmonic responses ($n = 2-6$), (b) *NSE* for structures with 20% interface debonding: symmetric (Fig. 18(a)) and asymmetric (Fig. 18(b)) configurations.

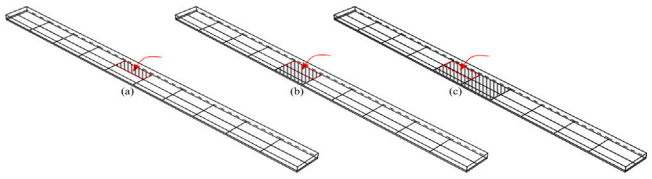

Fig. 23. Debonding of the layers' interface, indicated by hatching, at three fixed levels: (a) 5%, (b) 10%, and (c) 20%.

symmetric one exhibits a stronger superharmonic contribution and a higher *NSE*. Such behavior can be interpreted in terms of bending–extension coupling associated with the offset of the delamination from the neutral axis, which is a well-known effect in laminated structures. In qualitative terms, the observed trend is also in line with previous studies showing that the dynamic response of delaminated laminates depends on the position of the damage and the resulting changes in structural stiffness and deformation patterns [55].

4.2.3. Debonding size variation

This section examines the influence of debonding size by comparing three discrete sizes (Fig. 23). It is important to note that the debonding size remains constant throughout the analysis. Fig. 24 displays the temporal response for these cases, corresponding to the patterns shown in Fig. 23. The four subplots illustrate magnified time intervals within the 2-second analysis.

The results of Fig. 24 show a gradual change in the time-domain response with increasing delamination size, indicating a clear damage-scaling effect. While the responses are nearly identical at low excitation levels, larger delamination sizes introduce noticeable amplitude variations, phase shifts, and cycle irregularities, revealing enhanced nonlinear behavior. These observations suggest that damage-induced features may not be fully distinguishable in the time domain alone.

Fig. 25 represents the point-FRF plot for the debonded case studies in Fig. 23. Fig. 25 shows that increasing delamination size leads to limited minor frequency shifts in B_1 and B_2, while a more evident reduction is observed in B_3. This is attributed to the location of the damage near the turning point of the B_3 mode shape, where higher modal strain amplifies the effect of stiffness degradation. These findings are consistent with previous studies reporting stronger frequency sensitivity when damage is located in high-strain regions [9]. Moreover, T_1 shows a clear frequency reduction in all damaged cases relative to the pristine structure, with a noticeable separation between damage sizes. This indicates that torsional stiffness is affected not only by the presence of delamination but also by its extent. Such sensitivity of torsional modes to interfacial debonding is in accordance with previous experimental and numerical findings [8,9].

Table 1 summarizes the sensitivity of bending and torsional mode *FRF*s to variations in debonding size, pattern, and layup.

Table 1
Summary of *FRF* behavior for identifying damage-tracing modes at the turning points of mode shapes.

	Debonding size	Debonding pattern	Layup
Bending	✓	×	✓
Torsion	×	✓	✓

Fig. 26 shows the *FDE* over time for the debonded case studies in Fig. 23. Fig. 27(a)–(b) displays the η_n and *NSE* values for the damaged structures shown in Fig. 23.

Fig. 26 shows that the *FDE* does not increase monotonically with the extent of interlaminar debonding. Before excitation of the first bending mode (around $t \approx 0.75$ s), the 10% debonded configuration dissipates less energy than the 20% damaged case, owing to the larger effective contact length and earlier activation of frictional work for the wider debonding. As the excitation proceeds, the *FDE* curves intersect (around $t \approx 1$ s), and the 10% case ultimately exceeds the 20% case in terms of accumulated *FDE*. This inversion reflects a shift in the dominant interfacial regime: while the larger debonding initially enhances sliding near resonance, it also favors partial sticking or contact locking at later stages of the sweep, which progressively limits further frictional dissipation. By contrast, the intermediate debonding size preserves a more effective stick–slip balance over a wider excitation range.

This transition is consistently captured by the pseudo-modal damping distributions in Fig. 27. Near the fundamental resonance, the larger debonding (20%) shows a dominant contribution from the first harmonic, indicating that dissipation is mainly governed by the fundamental bending response. In contrast, the 10% debonded case exhibits a stronger first-superharmonic contribution, revealing a more efficient redistribution of energy from the fundamental response toward higher harmonics. Moreover, the relatively higher contributions of upper harmonics for the smaller debonding (e.g., 5%) underline the importance of accounting for higher-order harmonic components in damage assessment, as small debonding sizes may not manifest primarily at the fundamental frequency but rather through amplified responses at the first and second superharmonics ($2f_1$ and $3f_1$). Overall, increasing the debonding size modifies not only the magnitude of frictional dissipation but also its modal distribution, leading to a non-monotonic evolution of both *FDE* and η_n. A comparable counterintuitive dependence of modal damping on delamination size has also been reported experimentally for delaminated carbon-fiber-reinforced polymer laminates. To provide reference points for this behavior, Fig. 28 reports approximate modal damping variations replotted from Ref. [8].

5. Conclusion

This study proposed a hybrid time–frequency numerical framework to examine friction-induced modal dissipation in a delaminated beam. Unlike classical energy-based approaches that provide only aggregate

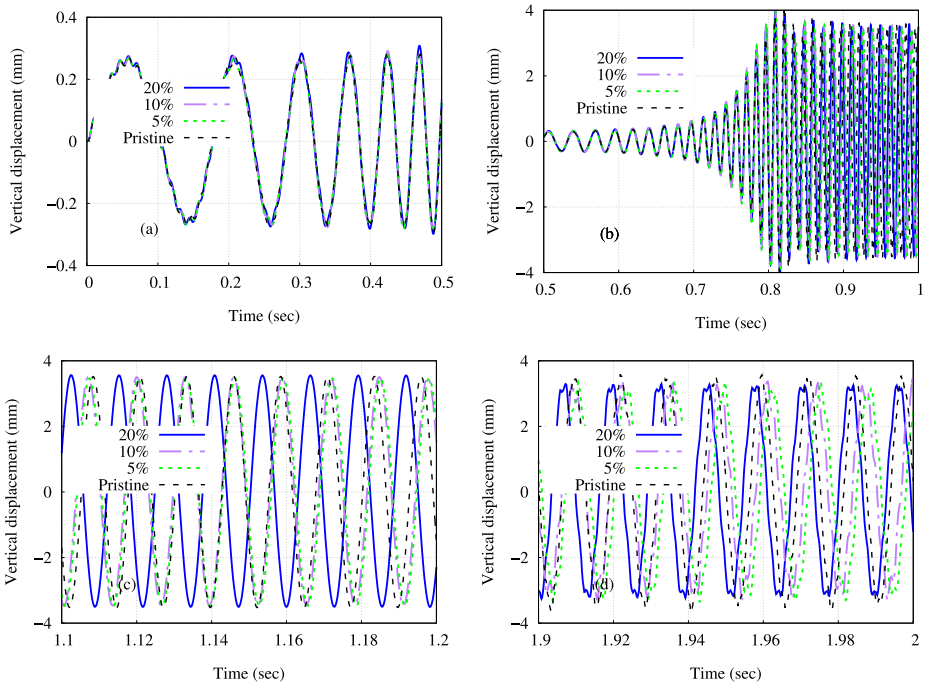

Fig. 24. Temporal history of the vertical displacement at the loading point for structures with fixed interface debonding of 5%, 10%, and 20% (Fig. 23(a)–(c)).

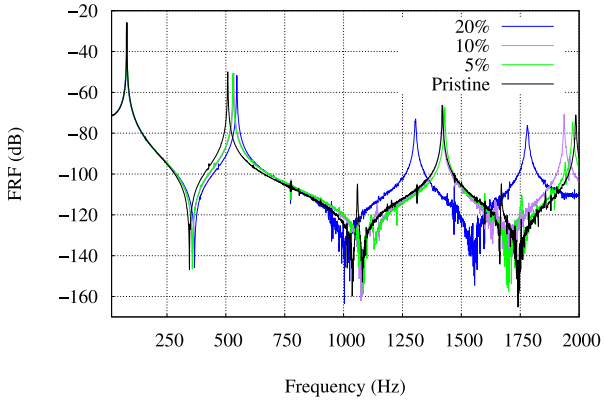

Fig. 25. Point–*FRF* of the structure with 20% interface debonding for structures with fixed interface debonding of 5%, 10%, and 20% (Fig. 23(a)–(c)).

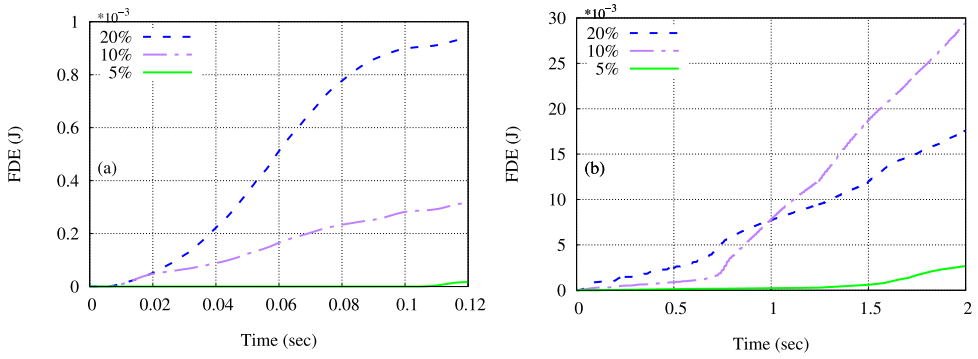

Fig. 26. Temporal *FDE* of the entire structure for structures with fixed interface debonding of 5%, 10%, and 20% (Fig. 23(a)–(c)).

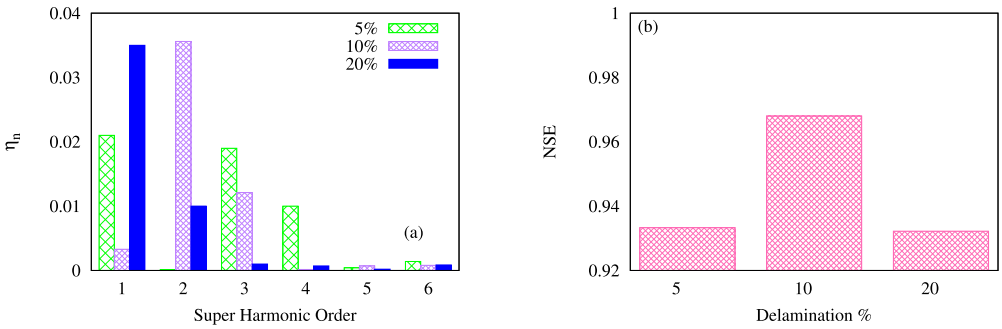

Fig. 27. (a) Distribution of the energy-based pseudo-modal dissipation index (η_n),computed for the fundamental mode ($n = 1$) and its first five superharmonic responses ($n = 2-6$), (b)*NSE* for structures with fixed interface debonding of 5%, 10%, and 20% (Fig. 23(a)–(c)).

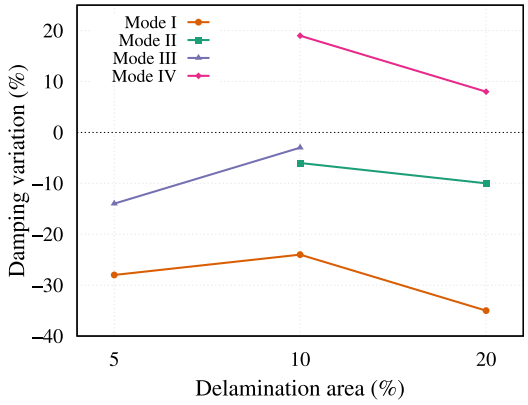

Fig. 28. Approximate modal damping variations with delamination area replotted from the experimental results reported in Ref. [8].

modal damping measures, the proposed method resolves the spectral contributions associated with nonlinear frictional response, including the fundamental component and its higher-order superharmonics. This enables a more physically grounded interpretation of modal damping variations induced by friction in debonded structures.

The coefficient of friction (*COF*) sensitivity analysis showed that, for the considered case study, varying the *COF* modifies both the interfacial slip regime and the spectral distribution of dissipation. In particular, the results revealed a non-monotonic dependence of η_n on *COF*, with dissipation remaining dominated by the low-order components, while the higher-order superharmonics become progressively suppressed.

The parametric analyses further showed that, for the considered beam configuration, the debonding geometry governs not only the magnitude of friction-induced dissipation, but also its modal and spectral distributions. The debonding pattern affects the coupling between friction and the dominant vibration mode. The position of the debonding relative to the neutral axis changes the balance between direct modal dissipation and superharmonic redistribution. Finally, the debonding size does not lead to a monotonic increase in frictional dissipation. Larger debondings may enhance sliding near resonance, but also tend to promote partial sticking at later stages of the frequency sweep, thereby limiting further dissipation, whereas intermediate sizes preserve a more effective stick–slip balance and promote a broader redistribution of energy toward superharmonic components.

Consistent with the previous experimental findings reported in [8] regarding the sensitivity of modal damping to damage, the present results support a mechanistic interpretation of friction-induced variations in modal dissipation in debonded structures. In this sense, the proposed framework may support future studies on damping-based damage characterization and on the interaction between friction-related and material-related dissipation mechanisms.

Future work

Future work will extend the present framework to other geometries and boundary conditions and will address the combined effect of interfacial friction and material-related dissipation mechanisms. The influence of excitation characteristics on the detectability of nonlinear effects induced by frictional contact will also be investigated.

CRediT authorship contribution statement

S. Kiasat: Writing – review & editing, Writing – original draft, Validation, Software, Methodology, Investigation, Formal analysis, Data curation, Conceptualization. **M. Filippi:** Writing – review & editing, Supervision. **Ali S. Nobari:** Writing – review & editing, Methodology. **E. Carrera:** Supervision.

Declaration of competing interest

The authors declare that they have no known competing financial interests or personal relationships that could have appeared to influence the work reported in this paper.

Data availability

Data will be made available on request.

References

[1] O. Allix, P. Ladevèze, Interlaminar interface modelling for the prediction of delamination, Compos. Struct. 22 (1992) http://dx.doi.org/10.1016/0263-8223(92)90060-P.
[2] P.P. Camanho, C.G. Davila, M.F. De Moura, Numerical simulation of mixed-mode progressive delamination in composite materials, J. Compos. Mater. 37 (16) (2003) http://dx.doi.org/10.1177/0021998303034505.
[3] H. Pakdel, B. Mohammadi, Stiffness degradation of composite laminates due to matrix cracking and induced delamination during tension-tension fatigue, Eng. Fract. Mech. 216 (2019) 106524, http://dx.doi.org/10.1016/j.engfracmech.2019.106489.
[4] A. Haeger, G. Schoen, F. Lissek, D. Meinhard, M. Kaufeld, G. Schneider, S. Schuhmacher, V. Knoblauch, Non-destructive detection of drilling-induced delamination in CFRP and its effect on mechanical properties, Procedia Eng. 149 (2016) 130–142, http://dx.doi.org/10.1016/j.proeng.2016.06.647.
[5] C. Colombo, T. Bhujangrao, F. Libonati, L. Vergani, Effect of delamination on the fatigue life of GFRP: A thermographic and numerical study, Compos. Struct. 218 (2019) 152–161, http://dx.doi.org/10.1016/j.compstruct.2019.03.023.
[6] O.S. Salawu, Detection of structural damage through changes in frequency: a review, Eng. Struct. 19 (9) (1997) 718–723, http://dx.doi.org/10.1016/S0141-0296(96)00149-6.
[7] D. Sharma, S.S. Gupta, R.C. Batra, Mode localization in composite laminates, Compos. Struct. 94 (8) (2012) 2620–2631, http://dx.doi.org/10.1016/j.compstruct.2012.02.023.
[8] M. Khazaee, A.S. Nobari, M.H.F. Aliabadi, Experimental investigation of delamination effects on modal damping of a CFRP laminate, using a statistical rationalization approach, in: Vibration-Based Techniques for Damage Detection and Localization in Engineering Structures, World Scientific, 2018, pp. 75–103, http://dx.doi.org/10.1142/9781786344977_0003.

[9] S. Kiasat, A.S. Nobari, M. Filippi, E. Carrera, Characterization of viscoelastic damping mechanism in a delaminated structure, Mech. Syst. Signal Process. 219 (2024) 111600, http://dx.doi.org/10.1016/j.ymssp.2024.111600.
[10] S. Kiasat, Novel approach to damage detection in laminated structures: modal damping as a damage indicator, Mater. Res. Proc. 42 (2024) http://dx.doi.org/10.21741/9781644903193-8.
[11] K. Popp, L. Panning, W. Sextro, Vibration damping by friction forces: theory and applications, J. Vib. Control 9 (3–4) (2003) 419–448, http://dx.doi.org/10.1177/107754603030780.
[12] P.R. Dahl, Solid friction damping of mechanical vibrations, AIAA J. 14 (12) (1967) 1675–1682, http://dx.doi.org/10.2514/3.61511.
[13] J.H. Griffin, A review of friction damping of turbine blade vibration, Int. J. Turbo Jet Eng. 7 (3–4) (1990) 297–308, http://dx.doi.org/10.1515/TJJ.1990.7.3-4.297.
[14] L. Gagnon, M. Morandini, G.L. Ghiringhelli, A review of friction damping modeling and testing, Arch. Appl. Mech. 90 (1) (2020) 107–126, http://dx.doi.org/10.1007/s00419-019-01600-6.
[15] P. Olejnik, Y.D. Desta, Friction-induced interactions: acoustic emissions, vibrations, and wear – a multiscale review, Nonlinear Dynam. 113 (2025) 24101–24140, http://dx.doi.org/10.1007/s11071-025-11397-5.
[16] Y. Yi, Y. Lei, L. J'ez'equel, X. Huang, A non-iterative method for nonlinear modal analysis of frictional systems using contact-state interpolation, Int. J. Non-Linear Mech. 180 (2026) 105254, http://dx.doi.org/10.1016/j.ijnonlinmec.2025.105254.
[17] M. Scheel, T. Schulz, M. Krack, Potential and limitation of a nonlinear modal testing method for friction-damped systems, in: Nonlinear Structures and Systems, Volume 1: Proceedings of the 37th IMAC, A Conference and Exposition on Structural Dynamics 2019, Springer, 2019, pp. 95–97.
[18] Y. Sun, J. Yuan, L. Pesaresi, E. Denimal, L. Salles, Parametric study and uncertainty quantification of the nonlinear modal properties of frictional dampers, J. Vib. Acoust. 142 (5) (2020) 051102, http://dx.doi.org/10.1115/1.4046953.
[19] Y. Sun, E. Denimal, J. Yuan, L. Salles, Geometric design of friction ring dampers in blisks using nonlinear modal analysis and Kriging surrogate model, Struct. Multidiscip. Optim. 65 (3) (2022) 98, http://dx.doi.org/10.1007/s00158-021-03093-w.
[20] S. Kiasat, A.S. Nobari, M. Filippi, Time-domain analysis of delaminated sandwich structures: Viscoelastic and frictional damping effects, Mech. Adv. Mater. Struct. (2025) 1–16, http://dx.doi.org/10.1080/15376494.2025.2535741.
[21] A. Klepka, M. Strączkiewicz, L. Pieczonka, et al., Triple correlation for detection of damage-related nonlinearities in composite structures, Nonlinear Dynam. 81 (2015) 453–468, http://dx.doi.org/10.1007/s11071-015-2004-6.
[22] M. Hammami, A. El Mahi, C. Karra, M. Haddar, Experimental analysis of the linear and nonlinear behaviour of composites with delaminations, Appl. Acoust. 108 (2016) 31–39, http://dx.doi.org/10.1016/j.apacoust.2015.10.026.
[23] A. Fantetti, D. Botto, S. Zucca, C. Schwingshackl, Guidelines to use input contact parameters for nonlinear dynamic analysis of jointed structures: Results of a round robin test, Tribol. Int. 191 (2024) 109158, http://dx.doi.org/10.1016/j.triboint.2023.109158.
[24] A. Fantetti, S. Mariani, L. Pesaresi, D. Nowell, F. Cegla, C. Schwingshackl, Ultrasonic monitoring of friction contacts during shear vibration cycles, Mech. Syst. Signal Process. 161 (2021) 107966, http://dx.doi.org/10.1016/j.ymssp.2021.107966.
[25] Z. Suo, J.W. Hutchinson, Interface crack between two elastic layers, Int. J. Fract. 43 (1) (1990) 1–18, http://dx.doi.org/10.1007/BF00018123.
[26] K.L. Johnson, Contact Mechanics, Cambridge University Press, 1987.
[27] P. Wriggers, T.A. Laursen, Computational Contact Mechanics, Springer, 2006, http://dx.doi.org/10.1007/978-3-540-32609-0.
[28] N. Kikuchi, J.T. Oden, Contact Problems in Elasticity: A Study of Variational Inequalities and Finite Element Methods, SIAM, 1988, http://dx.doi.org/10.1137/1.9781611970845.
[29] J.C. Simo, T.A. Laursen, An augmented Lagrangian treatment of contact problems involving friction, Comput. Struct. 42 (1) (1992) 97–116, http://dx.doi.org/10.1016/0045-7949(92)90540-G.
[30] P. Wriggers, C. Miehe, Contact constraints within coupled thermomechanical analysis—a finite element model, Comput. Methods Appl. Mech. Engrg. 113 (3–4) (1994) 301–319, http://dx.doi.org/10.1016/0045-7825(94)90051-5.
[31] H.W. Kuhn, A.W. Tucker, Nonlinear programming, in: Proceedings of the Second Berkeley Symposium on Mathematical Statistics and Probability, University of California Press, Berkeley, California, 1951, pp. 481–492, http://dx.doi.org/10.1007/978-0-387-76635-5_3.
[32] D. Li, C. Xu, J. Kang, Z. Zhang, Modeling tangential friction based on contact pressure distribution for predicting dynamic responses of bolted joint structures, Nonlinear Dynam. 101 (3) (2020) 255–269, http://dx.doi.org/10.1007/s11071-020-05765-6.
[33] K. Zong, Z. Qin, F. Chu, Modeling of frictional stick–slip of contact interfaces considering normal fractal contact, J. Appl. Mech. 89 (3) (2022) 031003, http://dx.doi.org/10.1115/1.4052882.
[34] P. Flores, Contact mechanics for dynamical systems: a comprehensive review, Multibody Syst. Dyn. 58 (1) (2022) 1–51, http://dx.doi.org/10.1007/s11044-021-09803-y.
[35] J. Carlberg, B. Toyib, Finite Element Modeling of Interlaminar Slip in Stress-Laminated Timber Decks, Friction Interaction Modeling using Abaqus (Master's thesis), Chalmers University of Technology, Göteborg, Sweden, 2012, Available at: https://hdl.handle.net/20.500.12380/162914.
[36] MathWorks, Spectral analysis, 2026, Available at: https://it.mathworks.com/help/signal/ug/spectral-analysis.html. (Accessed 16 February 2026).
[37] D.G. Martinson, Quantitative Methods of Data Analysis for the Physical Sciences and Engineering, Cambridge University Press, 2018, http://dx.doi.org/10.1017/9781139342568.
[38] A.R. Bansal, V.P. Dimri, Power spectral density, in: B. Daya Sagar, Q. Cheng, J. McKinley, F. Agterberg (Eds.), Encyclopedia of Mathematical Geosciences, Springer, 2021, pp. 1–3, http://dx.doi.org/10.1007/978-3-030-26050-7_254-1.
[39] E. Sauther, Sine Sweep Vibration Testing for Modal Response Primer, Department of Optical Sciences, University of Arizona, Tucson, 2013.
[40] T. Irvine, Sine sweep testing, 2023, enDAQ. Available at: https://endaq.com/pages/sine-sweep-testing. (Accessed 9 April 2025).
[41] A.U. Mange, J. Zhao, Sine Sweep in High Frequency Range, Sentek Dynamics, 2021, Available at: https://www.sentekdynamics.com/sentek-dynamics-news/2021/9/21/sine-sweep-in-high-frequency-range. (Accessed 9 April 2025).
[42] S. Kiasat, A.S. Nobari, M. Filippi, E. Carrera, Investigating the effect of delamination-induced frictional contact on the dynamic behavior of laminate structures, in: Proceedings of the 34th Congress of the International Council of the Aeronautical Sciences, ICAS, Florence, Italy, 2024.
[43] Z. Reches, Constraints on the strength of the upper crust from stress inversion of fault slip data, J. Geophys. Res.: Solid Earth 97 (B9) (1992) 12481–12493, http://dx.doi.org/10.1029/90JB02258.
[44] C. Touzé, M. Amabili, Nonlinear normal modes for damped geometrically nonlinear systems: Application to reduced-order modelling of harmonically forced structures, J. Sound Vib. 298 (4–5) (2006) 958–981.
[45] A. Meziane, A.N. Norris, A.L. Shuvalov, Nonlinear shear wave interaction at a frictional interface: Energy dissipation and generation of harmonics, J. Acoust. Soc. Am. 130 (4) (2011) 1820–1828, http://dx.doi.org/10.1121/1.3629360.
[46] A.A. Ferri, E.H. Dowell, Frequency domain solutions to multi-degree-of-freedom, dry friction damped systems, J. Sound Vib. 124 (2) (1988) 207—224, http://dx.doi.org/10.1016/S0022-460X(88)80183-4.
[47] J.J. Chen, B.D. Yang, C.H. Menq, Periodic forced response of structures having three-dimensional frictional constraints, J. Sound Vib. 229 (4) (2000) 775–792, http://dx.doi.org/10.1006/jsvi.1999.2397.
[48] M. Krack, J. Gross, Harmonic Balance for Nonlinear Vibration Problems, Springer, 2019, http://dx.doi.org/10.1007/978-3-030-14023-6.
[49] J.H. Porter, M.R.W. Brake, Tracking superharmonic resonances for nonlinear vibration of conservative and hysteretic single degree of freedom systems, Mech. Syst. Signal Process. 215 (2024) 111410, http://dx.doi.org/10.1016/j.ymssp.2024.111410.
[50] A.H. Nayfeh, D.T. Mook, Nonlinear Oscillations, Wiley, New York, 1979.
[51] R.A. Ibrahim, Friction-induced vibration, chatter, squeal, and chaos – Part I: Mechanics of friction, Appl. Mech. Rev. 47 (7) (2005) 209–253, http://dx.doi.org/10.1115/1.3111079.
[52] M. Groper, Microslip and macroslip in bolted joints, Exp. Mech. 25 (2) (1985) 171–174, http://dx.doi.org/10.1007/BF02328808.
[53] K. Worden, G.R. Tomlinson, Nonlinearity in structural dynamics: Detection, identification and modelling, Phil. Trans. R. Soc. A 359 (1781) (2001) 113–130, http://dx.doi.org/10.1201/9780429138331.
[54] N. Menga, G. Carbone, D. Dini, Exploring the effect of geometric coupling on friction and energy dissipation in rough contacts of elastic and viscoelastic coatings, J. Mech. Phys. Solids 148 (2021) 104273, http://dx.doi.org/10.1016/j.jmps.2020.104273.
[55] C. Yang, S.O. Oyadiji, Detection of delamination in composite beams using frequency deviations due to concentrated mass loading, Compos. Struct. 146 (2016) 1–13, http://dx.doi.org/10.1016/j.compstruct.2015.12.002.
[56] S. Bennati, P. Fisicaro, L. Taglialegne, P.S. Valvo, An elastic interface model for the delamination of bending–extension coupled laminates, Appl. Sci. 9 (17) (2019) 3560, http://dx.doi.org/10.3390/app9173560.

Further reading

[1] V. Birman, D.A. Saravanos, D.A. Hopkins, Sensory composite beams for delamination detection in thermal environments, ASME Int. Mech. Eng. Congr. Expo. 14581 (1994) 351–358.